Modeling Long Memory in 67 Million Years of Cyclical Climate Trends: Anticipating Future Cycles

Yeliz Özer*, Tomás del Barrio Castro†, Álvaro Escribano‡, Philipp Sibbertsen§

August 11, 2026

Abstract

Deep-time climate records contain deterministic orbital signals and persistent stochastic variation, but how these components jointly affect predictability across climate states remains unclear. We analyze the Cenozoic Global Reference benthic foraminifer oxygen and carbon isotope record spanning 67.1 million years. This very long period is divided into seven climate-state segments. For each segment, we estimate deterministic contemporaneous long-run components combining linear trends, eccentricity, obliquity, climatic precession, and identified harmonic frequencies. The remaining variation is modeled with a bivariate vector autoregressive forecasting framework conditioned on astronomical forcing. The selected deterministic and dynamic structures differ substantially across climate states. Obliquity is the most recurrent orbital predictor, whereas squared obliquity, eccentricity, climatic precession, and harmonic components contribute only in particular segments and differ between the two proxies. Forecast accuracy likewise varies across the record, although observed and predicted values agree closely in several segments. A projection for the next 100,000 years provides a baseline implied by natural astronomical forcing and continued Icehouse dynamics. Overall, the results show that orbital responsiveness, proxy interactions, and statistical predictability are state dependent. Deep-time climate variability therefore cannot be represented by a single common combination of deterministic forcing and stochastic dynamics across the complete Cenozoic.

Keywords: CENOGRID · Deep-Time Paleoclimate · Forecasting Climate Data.

JEL classification: C22 · C32 · C53

*Corresponding Author. Leibniz University Hannover, School of Economics and Management, Institute of Statistics, Königsworther Platz 1, D-30167 Hannover, Germany. E-Mail: oezer@statistik.uni-hannover.de. Phone: +49-511-762-3082

†Department of Applied Economics, Universitat de les Illes Balears, E-Mail: tomas.barrio@uib.es

‡Department of Economics, Universidad Carlos III de Madrid. E-Mail: alvaroe@eco.uc3m.es

§Leibniz University Hannover, School of Economics and Management, Institute of Statistics. E-Mail: sibbertsen@statistik.uni-hannover.de

1 Introduction

Deep-time climate records provide a unique archive of climate states spanning atmospheric greenhouse-gas concentrations both comparable to and substantially exceeding those of today. Consequently, they provide one of the few opportunities to observe how the Earth system responds to climatic conditions outside the range of instrumental observations and are increasingly used to evaluate Earth system models, constrain climate sensitivity, and improve our understanding of future climate under elevated atmospheric CO_2 concentrations (Tierney et al., 2020; Lunt et al., 2024; Braconnot et al., 2021). Developing statistical models that adequately describe these records is therefore important not only for reconstructing Earth's climate history, but also for improving our understanding of the long-term response of the climate system to different forcing mechanisms. Statistical models provide a complementary perspective by describing the underlying dynamics of paleoclimate records and assessing how well these dynamics translate into predictive performance.

From a statistical perspective, however, deep-time proxy records pose several challenges. They typically exhibit strong persistence, multiple cyclical components, structural changes associated with different climate states, and astronomical forcing. These characteristics complicate the application of conventional time-series models and make it difficult to separate deterministic from stochastic variation. While previous studies have identified dominant orbital periodicities and investigated persistence in paleoclimate records, recent statistical approaches have primarily focused on individual aspects such as long-memory behavior, orbital forcing, or forecasting (Castle and Hendry, 2020; del Barrio Castro et al., 2025). By comparison, no study has combined these features within a unified statistical framework for such a long time series or evaluated their joint contribution to modeling and forecasting.

In del Barrio Castro et al. (2026), the Cenozoic Global Reference benthic foraminifer carbon and oxygen isotope record has been analyzed using long-memory estimation, sequential frequency identification, frequency-specific unit-root and stationarity tests, and cyclical fractional cointegration. The analysis showed that the isotope records are characterized by persistent long-memory dynamics together with astronomical forcing and additional harmonic components whose importance varies across climate states. Furthermore, we showed that common spectral peaks do not necessarily imply stable long-run relationships, emphasizing that spectral similarity alone is insufficient to characterize the dependence structure of deep-time climate records.

Building on these findings, we investigate whether the identified deterministic components provide additional explanatory and predictive information. In particular, it remains unclear to what extent the observed variation can be explained by deterministic trends, orbital forcing, and harmonic components, and how much should instead be modeled as stochastic. Answering this question is relevant not only for improving the statistical description of paleoclimate proxy records but also for assessing the statistical predictability of deep-time climate dynamics.

To address these questions, we develop a segment-specific modeling framework for the long-run component of the isotope records by combining deterministic trends, contemporaneous astronomical forcing variables, and the harmonic frequencies identified in del Barrio Castro et al. (2026). The remaining stochastic component is dynamically modeled and evaluated through in-sample and out-of-sample forecasting. For the out-of-sample forecasting we compare our findings with those of del Barrio Castro et al. (2025). This decomposition allows us to quantify the contribution of deterministic climate forcing to the observed variability and to assess how well the identified statistical structure translates into forecasting performance. Rather than proposing a physical climate model, our objective is to investigate the statistical predictability of deep-time climate variability within a frequency-based time-series framework.

The remainder of the paper is organized as follows. Section 2 briefly introduces the data. Section 3 presents the long-run deterministic cyclical trending modeling, while section 4 develops the stochastic dynamic modeling and forecasting framework. Finally, section 5 discusses the overall results and the main conclusions.

2 Data description of δ^{18}O, δ^{13}C, and orbital variables

The analysis is based on the Cenozoic Global Reference benthic foraminifer carbon and oxygen isotope record developed by Westerhold et al. (2020), covering the past 67.1 million years (Myr)[1]. We use the interpolated benthic δ^{18}O and δ^{13}C series. The δ^{18}O record reflects variations in deep-ocean temperature and continental ice volume, whereas δ^{13}C contains information on changes in the global carbon cycle and ocean circulation. The published CENOGRID series are available at 5-kyr intervals for the Paleocene and Eocene and at 2-kyr intervals from the Oligocene to the present. Following del Barrio Castro et al. (2026), we use a uniformly interpolated 5-kyr grid for the complete record. We further use the cleaned proxy series obtained in that study. The cleaning accounts for the main event-related deviations around the Paleocene–Eocene Thermal Maximum using indicator saturation. The resulting adjustments are confined to a short interval around 56 Ma, while the remainder of the record is unchanged.

To allow the statistical relationships to differ across background climate states, both proxies are divided into the seven segments identified from the climate-state transitions in Westerhold et al. (2020). The segment boundaries are located at approximately 56, 47, 34, 13.9, 7, and 3.3 Ma, separating the Warmhouse, Hothouse, Coolhouse, and Icehouse states shown in Fig. 1. Although the transition at 7 Ma is more distinct in δ^{13}C than in δ^{18}O, the same segmentation is applied to both proxies to maintain a common system for the subsequent multivariate analysis. Further details on the interpolation, cleaning procedure, and segmentation are provided in del Barrio Castro et al. (2026).

[1]Million annum (Ma) refers to an absolute time point in the past, whereas million years (Myr) and thousand years (kyr) denote time spans or durations.

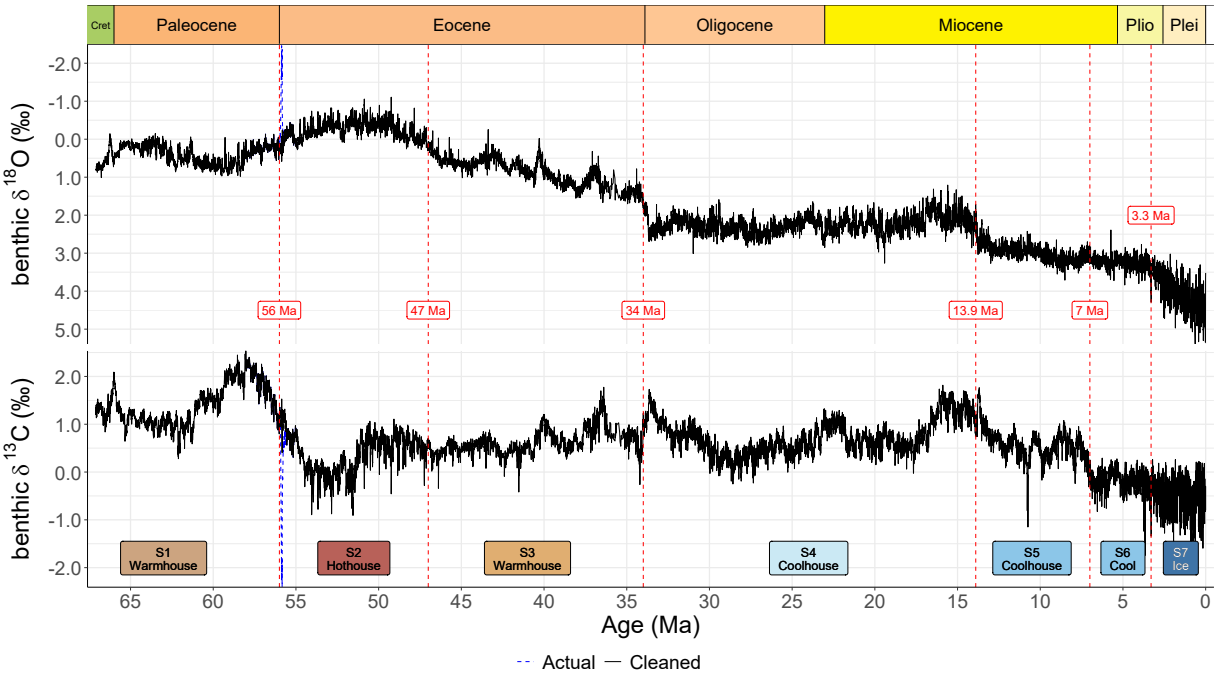

Figure 1: Interpolated equidistant δ^{18}O and δ^{13}C, with breaks according to Westerhold et al. (2020) in δ^{13}C.

The astronomical regressors consist of eccentricity, obliquity, and climatic precession. Eccentricity is taken from the La2010b solution used for the astronomical tuning of CENOGRID, while obliquity and climatic precession are obtained from the La2004 solution (Laskar et al., 2004; Westerhold et al., 2020). In addition to the individual orbital variables, the models include the interaction between eccentricity and obliquity and squared obliquity to allow for combined and nonlinear effects. Climatic precession is defined as $e\sin(\varpi)$. The use of astronomical solutions in deeper time is subject to increasing uncertainty because the available orbital solutions diverge as a result of chaotic Solar System dynamics. A comparison of the residual series obtained from alternative astronomical inputs is provided in Fig. 6 in the Appendix.

3 Detrending deep-time paleoclimate data

We estimate the deterministic trend in each cleaned proxy (δ^{18}O and δ^{13}C) within the previously defined seven segments. The goal of this step is to separate the orbitally forced and long-term deterministic components from the remaining variability, which is modeled in the subsequent analysis.

Let $\mathbf{Y}_{s,t} = [\delta^{18}\mathrm{O}_{s,t},\ \delta^{13}\mathrm{C}_{s,t}]'$ denote the vector of cleaned proxies for segment $s \in \{1,\dots,7\}$ and local segment-specific time index t. We model $\mathbf{Y}_{s,t}$ as a linear combination of a linear trend term, orbital parameters, and harmonic frequencies:

$$\begin{aligned}\mathbf{Y}_{s,t} = \boldsymbol{\beta}_{0,s} + \boldsymbol{\beta}_{1,s}\,\mathrm{trend}_{s,t} + \boldsymbol{\beta}_{2,s}\,ecc_{s,t} + \boldsymbol{\beta}_{3,s}\,eccob_{s,t} + \boldsymbol{\beta}_{4,s}\,ob_{s,t} \\ + \boldsymbol{\beta}_{5,s} ob^2_{s,t} + \boldsymbol{\beta}_{6,s} pre_{s,t} + \sum_{a=1}^{k}[\mathbf{a}_{a,s}\cos(\omega_a t) + \mathbf{b}_{a,s}\sin(\omega_a t)] + \boldsymbol{\epsilon}_{s,t},\end{aligned} \tag{1}$$

where $\boldsymbol{\epsilon}_{s,t}$ denotes the residual term and $\mathrm{trend}_{s,t}$ represents the local linear trend within each segment s. All coefficients in Eq. (1) are estimated jointly by ordinary least squares (OLS). The harmonic frequencies ω_α are taken from del Barrio Castro et al. (2026), where the proxy series were linearly detrended prior to frequency identification to separate low-frequency deterministic trend variation from cyclical components.

Following the specification strategy proposed by Castle and Hendry (2020) and del Barrio Castro et al. (2025), we allow for alternative representations of astronomical forcing by considering different combinations of orbital variables. These include Earth's eccentricity ($ecc_{s,t}$), the interaction between eccentricity and obliquity ($eccob_{s,t}$), obliquity ($ob_{s,t}$), and squared obliquity ($ob^2_{s,t}$) to account for nonlinear effects. Since our interest lies in the climatic response to orbital forcing rather than in the purely astronomical representation of precession, we further include climatic precession ($pre_{s,t}$ defined as $e\,sin(\varpi)$) instead of the precession index, which is a circular variable.

The harmonic frequencies account for additional cyclic variability beyond the direct orbital parameters. Following del Barrio Castro et al. (2026), we include all identified angular frequencies for each segment, as listed in Tab. 1.

For each segment s, the parameter vector

$$\boldsymbol{\theta}_s = (\boldsymbol{\beta}_{0,s}, \boldsymbol{\beta}_{1,s}, \boldsymbol{\beta}_{2,s}, \boldsymbol{\beta}_{3,s}, \boldsymbol{\beta}_{4,s}, \boldsymbol{\beta}_{5,s}, \boldsymbol{\beta}_{6,s}, \mathbf{a}_{1,s}, \mathbf{b}_{1,s}, \ldots, \mathbf{a}_{k,s}, \mathbf{b}_{k,s})$$

is estimated via OLS. Model selection is performed separately for each segment using an automated stepwise Bayesian information criterion (BIC) procedure on all independent variables except the constant and linear trend. Coefficients corresponding to predictors dropped by the BIC are set to zero.

The fitted values $\hat{\mathbf{Y}}_{s,t}$ are given by

$$\begin{aligned}\hat{\mathbf{Y}}_{s,t} = \hat{\boldsymbol{\beta}}_{0,s} + \hat{\boldsymbol{\beta}}_{1,s}\,\mathrm{trend}_{s,t} + \hat{\boldsymbol{\beta}}_{2,s}\,ecc_{s,t} + \hat{\boldsymbol{\beta}}_{3,s}\,eccob_{s,t} \\ + \hat{\boldsymbol{\beta}}_{4,s}\,ob_{s,t} + \hat{\boldsymbol{\beta}}_{5,s}\,ob^2_{s,t} + \hat{\boldsymbol{\beta}}_{6,s}\,pre_{s,t} + \sum_{a=1}^{k}\left[\hat{\mathbf{a}}_{a,s}\cos(\omega_a t) + \hat{\mathbf{b}}_{a,s}\sin(\omega_a t)\right].\end{aligned} \tag{2}$$

The residuals are defined as

$$\hat{\boldsymbol{\epsilon}}_{s,t} = \mathbf{Y}_{s,t} - \hat{\mathbf{Y}}_{s,t}. \tag{3}$$

The fitted values $\hat{\mathbf{Y}}_{s,t}$ capture the orbitally forced and trend-driven variation within each segment, while the residuals $\hat{\boldsymbol{\varepsilon}}_{s,t}$ represent the remaining fluctuations (Fig. 2). These residuals form the basis for the subsequent stochastic modeling and forecasting. The segment-specific regression results for both proxies are reported in Tab. 3 and Tab. 4 in the Appendix. Further, we provide two additional figures in the

Appendix: one shows the deterministic trend from segment 7 continued for the next 100 kyr (Fig. 5). The other shows that the differences in the residuals caused by using different astronomical solutions are negligible for the most recent segments (Fig. 6).

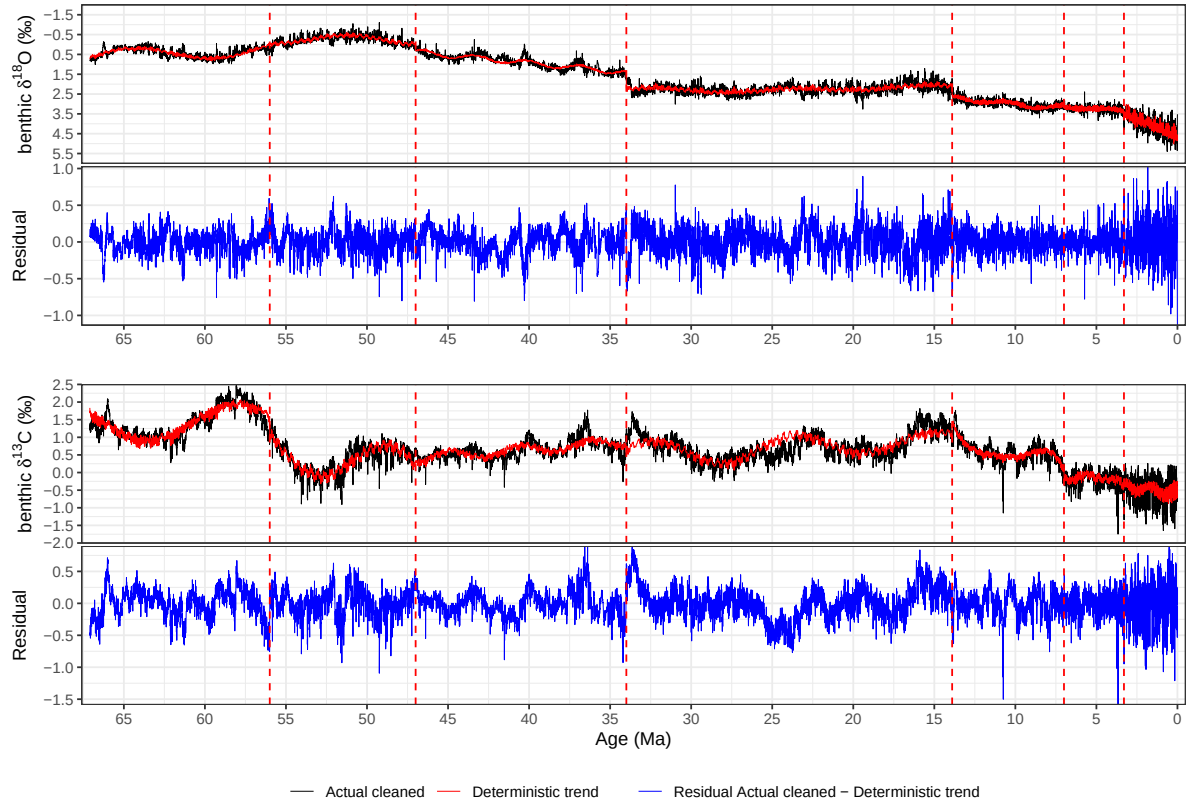

Figure 2: Interpolated equidistant cleaned δ^{18}O and δ^{13}C, with deterministic trend, residuals; with breaks according to Westerhold et al. (2020) in δ^{13}C.

Taken together, the segment-wise results in Tab. 3 and 4 show that the deterministic component of both isotope series is strongly regime dependent. The orbital contribution varies across segments and between δ^{18}O and δ^{13}C, and no single orbital variable is present in every specification. Nonetheless, some robust patterns emerge. Obliquity is the most persistent orbital component across the sample. Although it is not included in every individual equation, it appears in at least one of the two proxy equations in each segment and is selected jointly in both proxies until the Eocene-Oligocene transition, the mid- and late Coolhouse (Segments 1, 2, 3, 5, and 6). Squared obliquity is also prominent, especially in the early Cenozoic until nearly the end of the Miocene (Segments 1–5), but it is no longer retained in the last Cool- and Icehouse (Segments 6 and 7). Eccentricity contributes more intermittently, with a stronger role in δ^{18}O in the later segments, particularly Segments 6 and 7, and in δ^{13}C mainly in Segments 1 and 4. Climatic precession is only selected for δ^{18}O, and only in the most recent segments, indicating that its influence is both proxy- and regime-specific. Because the orbital variables are measured on different scales, the coefficients are not directly comparable in magnitude; we therefore focus on their recurrence across segments rather than on absolute coefficient size.

The same regime dependence is apparent in the harmonic components. No single trigonometric frequency is selected throughout every regime. However, very low-frequency harmonic components, with angular frequencies close to zero, recur across many segments in at least one of the two proxy equations. These terms therefore represent the most persistent harmonic contribution to the deterministic component and point to the importance of slow cyclical variability beyond the directly included orbital parameters. By contrast, higher-frequency terms, including frequencies close to the obliquity and precession bands, are selected only in particular segments. This suggests that these shorter cyclical components are expressed differently across climatic regimes. Segment 7 is also distinctive in showing a more restricted harmonic representation, with only cosine terms retained.

In summary, these findings indicate that the deterministic structure of the CENOGRID isotope series cannot be described by a common orbital specification across all segments. Instead, both the orbital variables and the harmonic terms contributing to the deterministic component vary across segments, consistent with a regime-dependent response of the climate system over the Cenozoic.

4 Modeling and forecasting δ^{18}O and δ^{13}C

For the in-sample and out-of-sample forecasting, we base our analysis on the previously obtained residuals from the segment-wise trend regressions. The dynamic interaction between the residuals of δ^{18}O and δ^{13}C is modeled using a reduced-form vector autoregressive (VAR) framework, which provides a standard tool for multivariate time series modeling and forecasting (Chevillon et al., 2018; Bauwens et al., 2023). In line with the interpretation of the paleoclimate system as a high-dimensional dynamic process, the reduced bivariate residual system can be viewed as a marginalized representation of a much larger underlying network. From a forecasting perspective, the model is therefore not intended as a structural description of the climate system, but rather as a feasible reduced-form approximation that preserves the dominant predictive features at the time scales under consideration. This interpretation links directly to the marginalization results in Chevillon et al. (2018) and Bauwens et al. (2023). From a time series standpoint, marginalization over omitted variables typically induces richer low-dimensional dynamics, including higher-order autoregressive behavior and moving-average components. Finite-order VAR models can thus be understood as practical approximations to the marginal dynamics of a larger system, which motivates their use when the primary objective is short-horizon predictive adequacy rather than structural interpretation.

Building on this argument and following del Barrio Castro et al. (2025), we employ a reduced-form VAR(2) model specification and extend it with astronomical variables to capture non-stochastic cyclicity. In systems exhibiting cyclical adjustment and delayed feedback effects, allowing for more than one lag is essential: a VAR(2) specification represents the lowest-order vector autoregressive model capable of

generating cyclical dynamics in the conditional mean. Accordingly, VAR(1) models are often too restrictive to capture the phase dynamics of persistent cyclical systems, whereas VAR(2) specifications provide a substantially better approximation to the underlying marginal process and improved short-horizon forecasting performance. This argument is particularly relevant for deep-time paleoclimate data, where oscillatory behavior induced by Milankovitch cycles is an intrinsic feature of the observed proxy series.

When physically motivated predictors are available that can be treated as predetermined, the reduced-form VAR framework can be augmented by including these variables as conditioning information in the conditional mean. In the paleoclimate context, orbital variables such as eccentricity, obliquity, and precession evolve independently of the proxy variables at the horizons considered and can therefore be treated as given. Conditioning the stochastic proxy dynamics on orbital forcing allows the model to separate endogenous proxy interactions from exogenous astronomical influences, while maintaining a linear and tractable forecasting structure. This reduced-form forecasting perspective closely follows recent paleoclimate applications that combine VAR-type dynamics with orbital variables to assess predictive performance (del Barrio Castro et al., 2025).

4.1 Model specification and selection

Let

$$\hat{\boldsymbol{\epsilon}}_{s,t} = \left(\hat{\epsilon}_{s,t}^{(\delta^{18}O)},\ \hat{\epsilon}_{s,t}^{(\delta^{13}C)}\right)'$$

denote the bivariate vector of residuals obtained after removing the deterministic component (linear trend, orbital regressors, and selected harmonic terms) from the proxy series in segment $s \in \{1, \ldots, 7\}$, with t denoting the local segment-specific time index. The stochastic dynamics of $\hat{\boldsymbol{\epsilon}}_{s,t}$ are modeled by the following VAR(2) representation including orbital variables as conditioning information:

$$\hat{\boldsymbol{\epsilon}}_{s,t} = \boldsymbol{\alpha}_s + \boldsymbol{\Phi}_{1,s}\hat{\boldsymbol{\epsilon}}_{s,t-1} + \boldsymbol{\Phi}_{2,s}\hat{\boldsymbol{\epsilon}}_{s,t-2} + \boldsymbol{B}_{0,s}\mathbf{x}_{s,t} + \boldsymbol{B}_{1,s}\mathbf{x}_{s,t-1} + \boldsymbol{B}_{2,s}\mathbf{x}_{s,t-2} + \boldsymbol{\eta}_{s,t}, \tag{4}$$

where $\boldsymbol{\eta}_{s,t} = (\eta_{s,t}^{(\delta^{18}O)}, \eta_{s,t}^{(\delta^{13}C)})'$ denotes the residual vector of the conditional mean equations in segment s, and $\hat{\boldsymbol{\eta}}_{s,t}$ denotes the corresponding OLS residuals.

The vector of orbital variables is $\mathbf{x}_{s,t} = (ecc_{s,t}, eccob_{s,t}, ob_{s,t}, ob_{s,t}^2, pre_{s,t})'$. Eq. (4) is interpreted as a reduced-form approximation to the marginal dynamics of the proxy residuals conditional on orbital forcing within each segment. The parameter matrices $\boldsymbol{\Phi}_{1,s}$ and $\boldsymbol{\Phi}_{2,s}$ capture own- and cross-dependence between the proxy residuals, while the matrices $\boldsymbol{B}_{j,s}$ with $j \in \{0, 1, 2\}$ summarize the contemporaneous and lagged effects of orbital variables on the conditional mean. The intercept vector $\boldsymbol{\alpha}_s$ accounts for any remaining mean level in the residual system after detrending in segment s.

The VAR(2) system in equation (4) can be estimated equation-by-equation as a system of autoregressive distributed lag regressions, since each equation is conditioned on the same information set. We estimate

the unrestricted model by OLS and apply a general-to-specific reduction based on the BIC to obtain a parsimonious forecasting representation.

Crucially, the VAR(2) lag structure implied by $\mathbf{\Phi}_{1,s}$ and $\mathbf{\Phi}_{2,s}$ is kept fixed, reflecting the marginalization argument and the need to preserve the cyclical adjustment dynamics. The selection procedure is applied to the orbital regressors and the harmonic components. Harmonic frequencies identified through cointegration tests (results are shown in Tab. 2; see del Barrio Castro et al. (2026) for further details) of the form $\sin(\omega t)$ and $\cos(\omega t)$ were included in the initial specification for each segment but were excluded by the BIC for the final forecasting equations. This approach yields a feasible forecasting model that balances flexibility and parsimony and is well suited for iterative (dynamic) multi-step prediction. All final segment-wise VAR(2) specifications can be found in the Appendix.

4.2 Forecast design and evaluation

For each segment s, in-sample forecasting is carried out over horizons $h = 1, \ldots, H$ with $H = 100$, corresponding to the last 100 observations within each segment. For a given segment, the VAR(2) model is estimated once by OLS using the remaining observations in that segment. Starting from the initial conditions implied by the VAR(2) lag structure, forecasts over the evaluation window are obtained by iterating the estimated VAR(2) equations forward, where predicted residuals are used as inputs for subsequent horizons. These forecasts are obtained by iterating the estimated VAR(2) model forward while conditioning on the orbital variables. Due to the VAR(2) lag structure, the first two observations in each segment are used solely for initialization and do not enter the forecast evaluation.

For the out-of-sample forecasting, the model is fitted on the full segment 7 and the forecasting is performed over the next 100 kyr ($h = 1, \ldots, H$ with $H = 20$). Since these future projections cannot be evaluated using forecast error measures, we compare the results to the work of del Barrio Castro et al. (2025).

For completeness, reconstructed proxy forecasts are obtained by adding back the estimated deterministic component from the detrending step. Let $\hat{\mathbf{Y}}_{s,t}$ denote the fitted deterministic part of $\mathbf{Y}_{s,t}$ in segment s as defined in Section 3 (including the linear trend and the BIC-selected orbital and harmonic terms). The reconstructed forecast at horizon h is then given by

$$\widehat{\mathbf{Y}}_{s,t+h|t} = \hat{\mathbf{Y}}_{s,t+h} + \hat{\boldsymbol{\epsilon}}_{s,t+h|t}, \qquad h \geq 1,$$

where $\hat{\boldsymbol{\epsilon}}_{s,t+h|t}$ is the h-step-ahead forecast of the residual component obtained from iterating the selected VAR(2) equations. Forecast accuracy within each segment is summarized by the mean squared error (MSE), computed as the average squared forecast error over horizons $h = 1, \ldots, H$ of the iterated forecast path. For each segment and proxy, the respective MSE is reported below the forecasting plot. Fig. 3 shows the in-sample and Fig. 4 the out-of-sample forecasting results, including the MSE and 95 % prediction

bands, where applicable. To increase readability, only the forecasting horizon is shown in the plots.

4.3 Residual autocorrelation diagnostics

As a diagnostic for remaining serial dependence, we analyze the autocorrelation functions (ACFs) of the OLS residuals $\hat{\boldsymbol{\eta}}_{s,t}$ from the selected VAR(2) mean equations. To obtain a statistically coherent assessment across lags, we employ simultaneous inference bands for autocorrelations as proposed by Hassler et al. (2025). Unlike conventional pointwise reference bands, simultaneous bands control the joint coverage probability of the entire ACF up to a specified maximum lag. Under the null hypothesis of white noise, the probability that all autocorrelations remain within the band is asymptotically equal to $1 - \alpha$. According to Hassler et al. (2025), the resulting ACFs provide a unified diagnostic: if any estimated autocorrelation leaves the simultaneous band, the white-noise hypothesis is rejected at level α for the ACF as a whole. In our analysis, we choose $\alpha = 0.05$. The simultaneous ACF bands indicate that residual serial dependence is substantially reduced for the BIC-selected specifications fully in segments 6, 7 and the out-of-sample period. Further partly in segment 5 for δ^{18}O, supporting the adequacy of the conditional mean dynamics used for the iterated forecasting exercise, at least in these segments (see Fig. 7).

4.4 Forecasting models of detrended δ^{18}O and δ^{13}C

The dynamic forecasting models based on detrended δ^{18}O and δ^{13}C residuals, reported in Tab. 5 and 6, show that the dynamic structure of the proxy residuals is strongly regime dependent. Although all segments are estimated within a common VAR(2) framework, the BIC-selected orbital regressors differ markedly across regimes, and the harmonic terms are excluded from the dynamic residual equations since they are already captured as part of the deterministic trend specification. Segment 1 is dominated by obliquity and squared obliquity in both proxy equations, whereas Segment 2 retains orbital forcing only in the δ^{13}C equation, and Segment 3 only in δ^{13}C through eccentricity–obliquity interaction, obliquity, and squared obliquity. Segment 4 splits the forcing structure across proxies, with obliquity, squared obliquity, and precession in δ^{18}O and eccentricity–obliquity interaction in δ^{13}C. Segment 5 combines eccentricity and eccentricity–obliquity interaction in δ^{18}O with obliquity and squared obliquity in δ^{13}C. Segments 6 and 7 are much sparser, with only isolated obliquity- or precession-related terms retained. Thus, the orbital drivers are not the same across segments, and only obliquity appears in every segment at least once, making it the most robust orbital predictor overall. The dynamics also vary substantially across regimes, with stronger persistence and better fit in the earlier and middle segments and weaker, sparser, and more selective dynamics in the late segments.

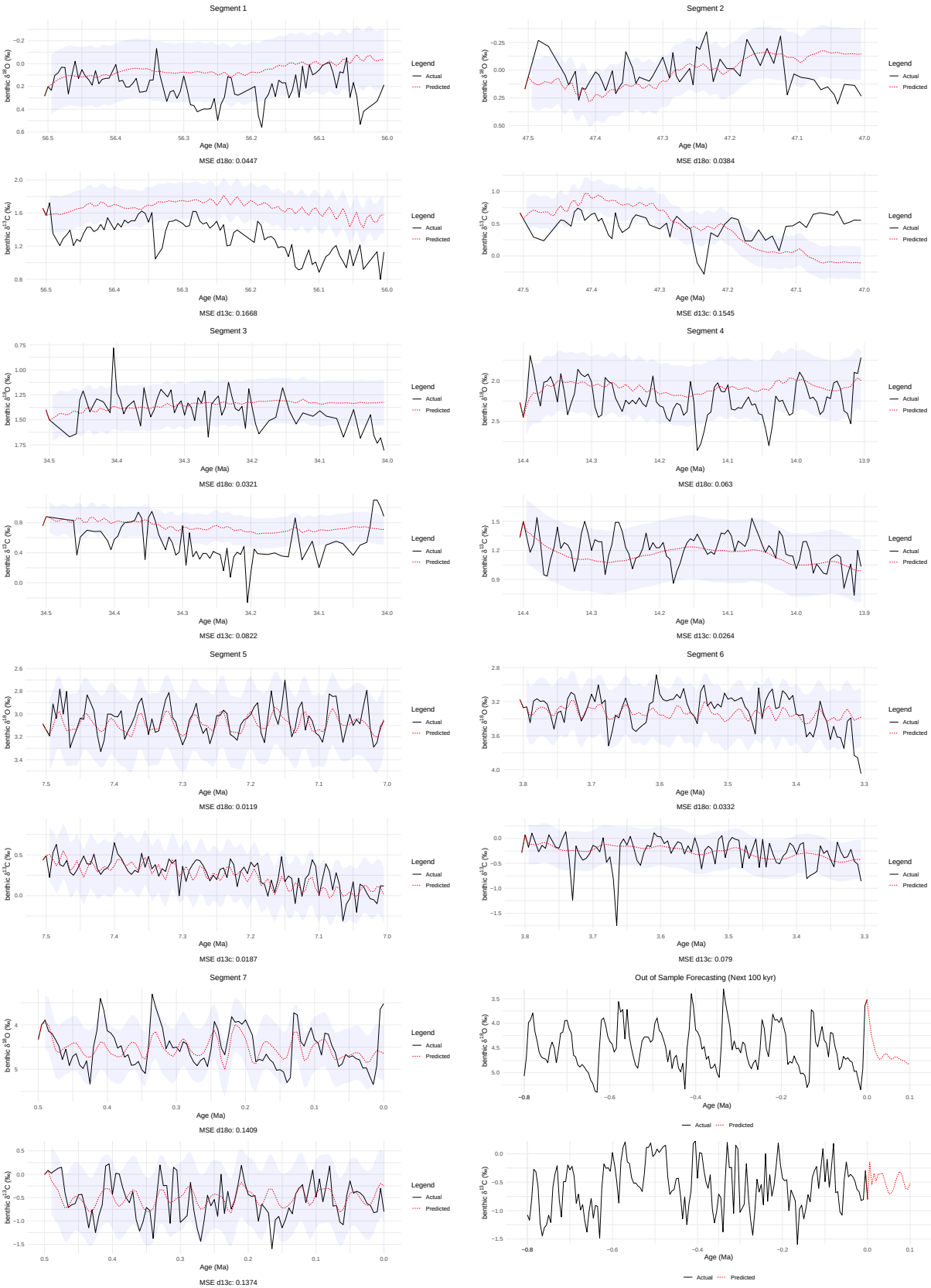

Figure 3: Segment-wise forecasting of δ^{18}O (top) and δ^{13}C (bottom), Segments 1–7 and Out-of-sample (next 100 kyr).

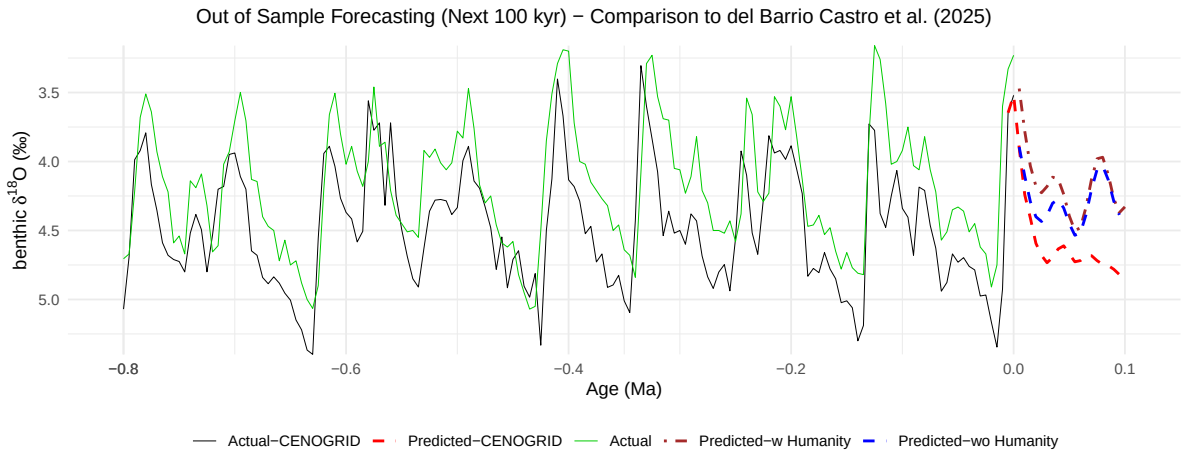

Figure 4: Out-of-sample Forecasting (Next 100 kyr) of δ^{18}O and Comparison to δ^{18}O of del Barrio Castro et al. (2025).

5 Discussion and conclusion

This paper examines how deterministic trends, astronomical forcing, and stochastic dynamics contribute to the variation and predictability of the Cenozoic benthic δ^{18}O and δ^{13}C records. The results show that neither the deterministic component nor the remaining proxy dynamics can be described by a single model for the whole Cenozoic. Instead, their statistical structure changes across the seven climate-state segments.

The segment-wise deterministic models reinforce this regime-based interpretation. The selected orbital regressors vary markedly across climate states, and no fixed forcing specification describes both proxies throughout the record. Obliquity is the most recurrent orbital component, appearing in at least one proxy equation in every segment. Squared obliquity is mainly retained in the early and middle Cenozoic, whereas climatic precession becomes relevant only in the later segments, particularly for δ^{18}O. Eccentricity and the eccentricity–obliquity interaction contribute less consistently and differ in importance between the two proxies.

These changes indicate that the statistical response to astronomical forcing depends on the prevailing climate state. However, the results do not establish a causal ranking of the orbital variables. The regressors are measured on different scales and partly contain related information, so their coefficient magnitudes are not directly comparable. The changing composition of the selected models is therefore more informative than the absolute size of individual coefficients. A full-sample specification would combine relationships that differ substantially across climate states and could obscure these changes in orbital responsiveness.

The trigonometric terms show a similar pattern. No exact harmonic frequency is selected in every segment, although very low-frequency sine and cosine components recur in several specifications. These terms capture slow variation that is not fully represented by the linear trends or the directly included orbital

variables. Their recurrence indicates that long-period variation is an important part of the deterministic structure of the isotope records. Nevertheless, their physical interpretation remains uncertain, particularly when the implied period approaches or exceeds the length of an individual segment. In such cases, a harmonic term may also approximate gradual nonlinear change. We therefore interpret these components primarily as part of the statistical decomposition rather than as evidence for a separate physical cycle in every case.

The results extend the frequency-specific analysis in del Barrio Castro et al. (2026), which identified persistent dependence, astronomical frequencies, and additional cyclical components whose importance varies across climate states. The present analysis shows that including these components in the deterministic models explains an important part of the observed variation. However, the deterministic decomposition does not fully account for the dynamics of the isotope records. Long-term trends, astronomical forcing, interactions between the proxies, and stochastic dynamics jointly contribute to the observed behavior.

The segment-wise forecasting models reported in Tab. 5 and Tab. 6 lead to the same general conclusion. Although all segments are modeled within a common VAR(2) framework, the selected orbital regressors and the own- and cross-proxy dynamics differ substantially. The harmonic terms are excluded from the final forecasting equations by the BIC, indicating that their contribution is mainly captured in the preceding deterministic decomposition. Earlier and middle Cenozoic segments generally show stronger interaction between δ^{18}O and δ^{13}C and higher explanatory power, whereas the specifications for the late Coolhouse and Icehouse are considerably sparser.

Obliquity is again the only orbital variable that appears in at least one forecasting equation in every segment, making it the most recurrent predictor across the dynamic models. Its presence does not, however, imply uniform forecasting performance. Forecast errors vary considerably across segments and proxies. Some middle Cenozoic segments produce comparatively accurate predictions, while performance is weaker in the most recent segment and for δ^{13}C in parts of the earlier record. Taken together, the variation in model structure and forecast accuracy points to state-dependent rather than uniform predictability.

The climatic response to the same astronomical forcing need not be identical in a largely ice-free Warmhouse, a transitional Coolhouse, and an Icehouse with substantial continental ice. Changes in ice volume, ocean circulation, carbon storage, and associated feedbacks may alter both the expression of orbital forcing and the relationship between δ^{18}O and δ^{13}C. The changing cross-proxy dynamics are consistent with this interpretation. The reduced-form framework does not identify the underlying physical mechanisms separately, but it shows that the statistical relationships between forcing, proxy dynamics, and predictability are not constant through time.

The projection for the next 100 kyr must be interpreted within this statistical framework. It is conditional on the continuation of the relationships estimated for Segment 7, on the selected astronomical solution, and on the absence of a further structural change. The model does not include future greenhouse-gas

concentrations or anthropogenic forcing. The projected path should therefore not be understood as an unconditional forecast of the future climate system, but as a baseline implied by natural astronomical variation and continued Icehouse dynamics. The comparison with del Barrio Castro et al. (2025) illustrates how different treatments of deterministic and stochastic components affect the resulting long-horizon projection.

In conclusion, the Cenozoic isotope records cannot be described by a common specification of astronomical forcing and stochastic dynamics across the complete Cenozoic. Obliquity is the most recurrent orbital predictor, but its role differs across proxies and climate states. The selected harmonic components, the interaction between δ^{18}O and δ^{13}C, and forecast performance likewise vary across the record. At the same time, the close agreement between observed and predicted values in several segments is noteworthy, especially since even visually noticeable deviations remain small in absolute terms. Climate memory, orbital responsiveness, and statistical predictability should therefore not be treated as fixed properties of the Cenozoic climate system. Accounting for these differences across climate states is important for modeling and assessing the predictability of deep-time paleoclimate records.

Acknowledgments

We thank Richard T. Baillie, Bärbel Hönisch, Norbert Marwan, Hashem Pesaran, Thomas Westerhold and James Zachos for inspiring discussion and comments on the paper. We further thank the participants of the XVI Workshop in Time Series Econometrics in Zaragoza, the General Assembly of the European Geosciences Union 2026, and the Climate and Energy Finance Conference at the Universidad Pontificia de Comillas in 2026 for helpful feedback.

Funding

Tomás del Barrio Castro gratefully acknowledges financial support from Grant PID2023-150095NB-C43, funded by MICIU/AEI/10.13039/501100011033 and, as appropriate, by "ERDF A way of making Europe", "ERDF/EU", the "European Union", or the European Union NextGenerationEU/PRTR.AEI. Álvaro Escribano acknowledges the funding received from grants PID2019-104960GB-I00 and CEX2021-001181-M funded by MICIU/AEI/10.13039/501100011033.

Appendix

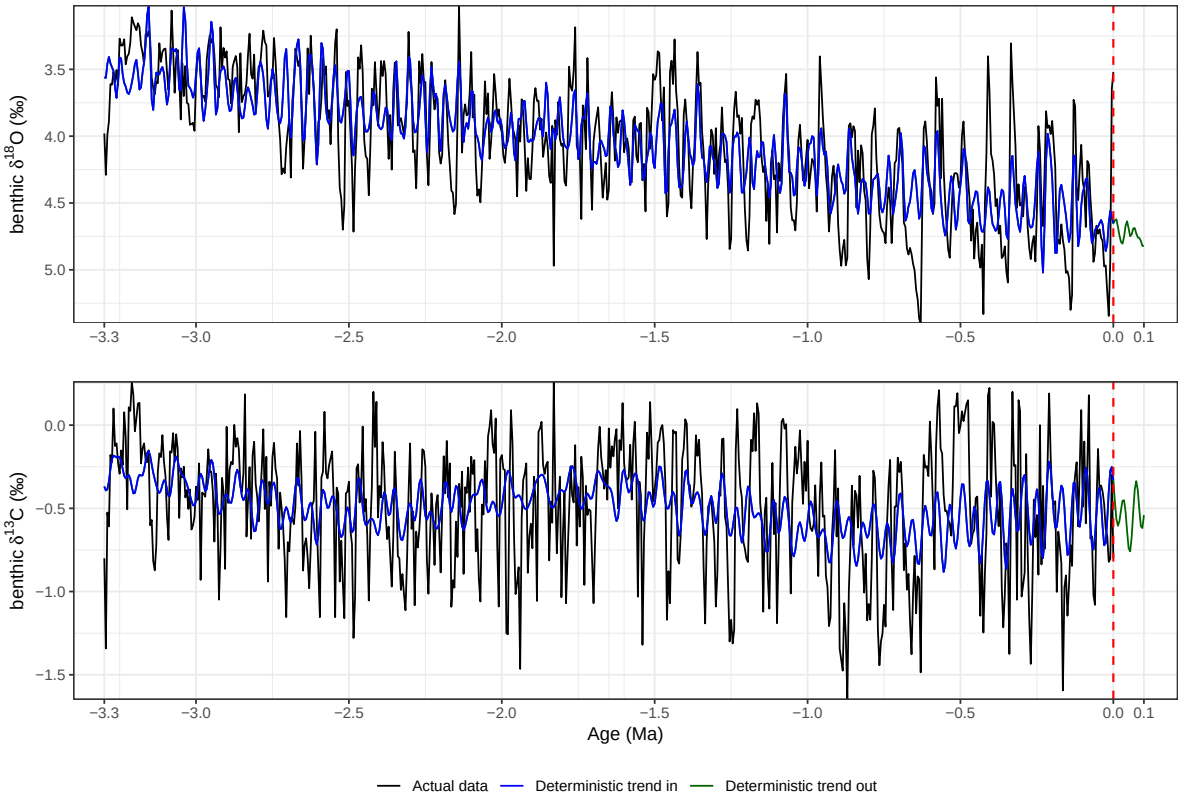

Figure 5: Deterministic trend for the past 800 kyr and the next 100 kyr (La2004).

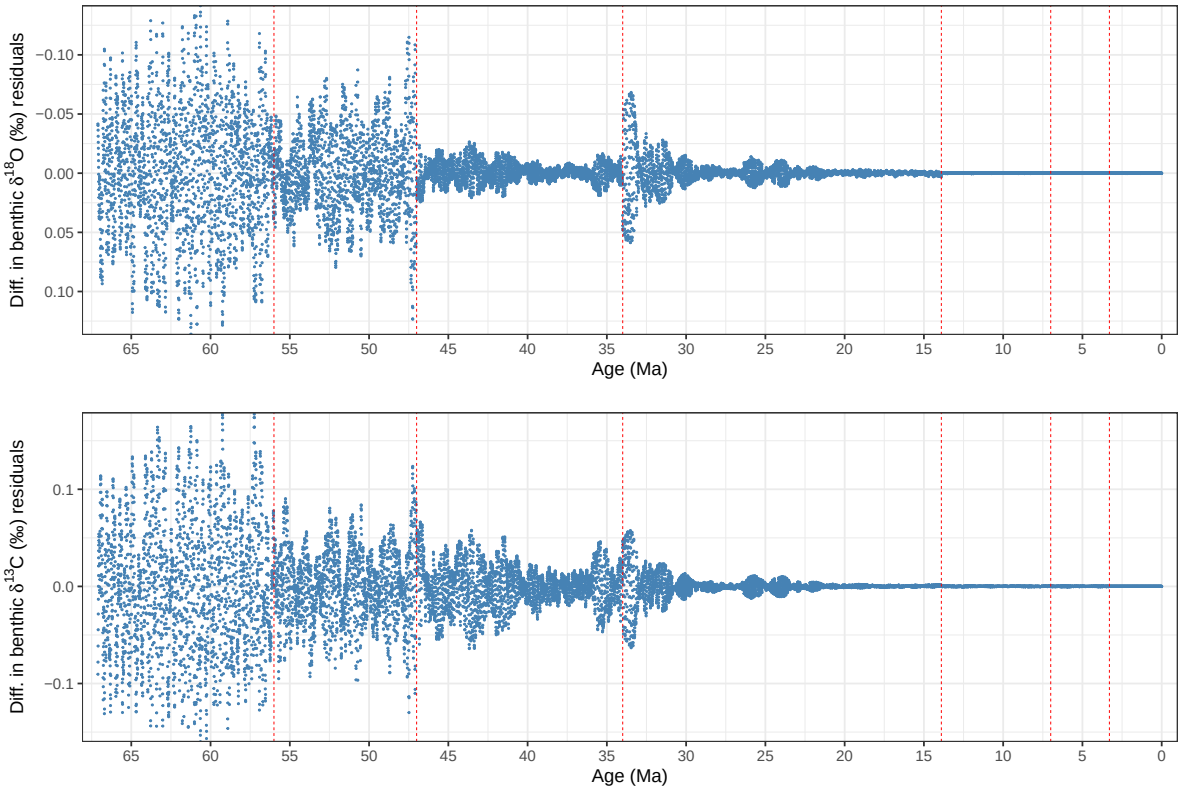

Figure 6: Differences in the residuals for the Cenozoic caused by using different astronomical solutions (La2004 vs. La2010b).

Table 1: Number of deterministic cycles, harmonic frequencies and degree of persistence (long-memory) in the equidistant (cleaned) CENOGRID.

	δ^{18}O	δ^{13}C
	Full Sample	
k	4	3
ω_a	0.0047 (6.7×10^3); 0.0778 (404); 0.7661 (41); 1.3279 (24)	0.0037 (8.4×10^3); 0.0778 (404); 0.7694 (41)
d_a	0.1893; 0.0282; 0.1815; 0.0655	0.259; 0.0608; 0.1266
	Segment 1	
k	2	1
ω_a	0.0028 (11.1×10^3); 2.3853 (13)	0.0028 (11.1×10^3)
d_a	0.3685; 0.0266	0.4091
	Segment 2	
k	3	3
ω_a	0.0035 (9×10^3); 0.3159 (99); 0.0777 (405)	0.0035 (9×10^3); 0.3159 (99); 0.0777 (405)
d_a	0.2132; 0.0823; 0.1590	0.2924; 0.1018; 0.2085
	Segment 3	
k	1	2
ω_a	0.0097 (3.3×10^3)	0.0072 (4.3×10^3); 0.2523 (125)
d_a	0.2555	0.3084; 0.0482
	Segment 4	
k	1	2
ω_a	0.0016 (20.1×10^3)	0.0031 (10.1×10^3); 0.0768 (409)
d_a	0.2261	0.3056; 0.2241
	Segment 5	
k	3	2
ω_a	0.0091 (3.5×10^3); 0.77 (41); 1.3275 (24)	0.0046 (6.9×10^3); 0.7843 (40)
d_a	0.145; 0.0369; 0.0551	0.3376; 0.0092
	Segment 6	
k	1	1
ω_a	0.7727 (41)	0.0085 (3.7×10^3)
d_a	0.066	0.0847
	Segment 7	
k	2	3
ω_a	0.77 (41); 0.2451 (128)	0.77 (41); 0.0193 (1.6×10^3); 0.3186 (99)
d_a	0.1419; 0.1721	0.0135; 0.0721; 0.1329
	67.1–34.005 Ma	
k	2	2
ω_a	0.0047 (6.62×10^3); 0.0779 (403)	0.0028 (11×10^3); 0.0779 (403)
d_a	0.2821; 0.1403	0.3025; 0.1314
	34–0 Ma	
k	1	3
ω_a	0.0037 (8.5×10^3)	0.0037 (8.5×10^3); 0.0777 (404); 0.7691 (41)
d_a	0.145	0.2487; 0.0828; 0.1278

Note: Model order (k), cyclical frequencies (ω_a) and memory parameters (d_a). Cycles are listed in the order of the iterative identification procedure; cycle lengths in kyr are given in parentheses.
Source: del Barrio Castro et al. (2026).

Table 2: Results for cyclical cointegration.

	$\hat{\beta}$	T^*	decision	d-b
Full Sample				
δ^{18}O - δ^{13}C - 0.0778 (404)	0.3124	5.3034	cointegration	0.1793
δ^{18}O - δ^{13}C - 0.77 (41)	0.1204	2.0434	cointegration	0.1461
δ^{18}O - ecc - 0.078 (403)	0.2854	4.8443	cointegration	0.1651
δ^{18}O - pre - 1.33 (24)	0.1205	2.0451	cointegration	0.1453
δ^{13}C - ecc - 0.078 (403)	0.2635	4.4734	cointegration	0.2042
δ^{13}C - ob - 0.77 (41)	-0.1968	-3.3406	cointegration	0.1602
Segment 2				
δ^{18}O - δ^{13}C - 0.0777 (404)	0.3371	3.1319	cointegration	0.1404
δ^{18}O - δ^{13}C - 0.3159 (99)	0.5369	4.9884	cointegration	-0.0109
δ^{18}O - ecc - 0.077 (408)	0.4539	4.2172	cointegration	0.0863
δ^{18}O - ecc - 0.3159 (99)	0.6097	5.6654	cointegration	-0.1241
δ^{13}C - ecc - 0.077 (408)	0.5203	4.8340	cointegration	-0.0137
δ^{13}C - ecc - 0.3159 (99)	0.7203	6.6924	cointegration	-0.303
Segment 4				
δ^{13}C - ecc - 0.077 (408)	0.5532	6.5409	cointegration	-0.012
Segment 5				
δ^{18}O - ob - 0.77 (41)	-0.3119	-2.6760	cointegration	-0.0132
Segment 6				
δ^{18}O - ob - 0.7727 (41)	-0.3545	-2.5228	cointegration	0.2247
67.1–34.005 Ma				
δ^{18}O - δ^{13}C - 0.0779 (403)	0.2963	4.0696	cointegration	0.1038
34–0 Ma				
δ^{18}O - δ^{13}C - 0.0037 (8.5×10^3)	0.1558	2.1571	cointegration	0.5946

Note: In parentheses, the identified cycle is shown in kyr.
Source: del Barrio Castro et al. (2026).

Segment-wise deterministic trend models

Table 3: Segment-wise deterministic long-run models for δ^{18}O. Deterministic segmented trend models with contemporaneous cyclical trends (deterministic and from orbital variables).

Regressor	Segment 1	Segment 2	Segment 3	Segment 4	Segment 5	Segment 6	Segment 7	Segment 7 (La2004)
Constant	43.2207	39.9934	-25.2907	-21.4122	-27.4443	5.3455	3.5888	3.5888
	(8.6633)	(9.7157)	(7.2337)	(6.6804)	(8.3061)	(0.2642)	(0.0335)	(0.0335)
Linear trend	-0.0003	0	0.0004	0	0.0004	0.0017	0.0018	0.0018
	(0)	(0)	(0)	(0)	(0)	(0.0003)	(0.0001)	(0.0001)
Eccentricity	-3.4882		-1.5351			-1.6684	227.0672	227.0478
	(0.2513)		(0.2527)			(0.3978)	(18.5756)	(18.5751)
Eccentricity × obliquity		-0.1060		-0.2290	-0.0853		-9.9604	-9.9596
		(0.0155)		(0.0104)	(0.0128)		(0.7961)	(0.7961)
Obliquity	-3.6637	-3.4782	2.2090	2.0711	2.7006	-0.1150		
	(0.7489)	(0.8389)	(0.6240)	(0.5756)	(0.7149)	(0.0105)		
Obliquity^2	0.0792	0.0752	-0.0474	-0.0449	-0.0602			
	(0.0162)	(0.0181)	(0.0135)	(0.0124)	(0.0154)			
Climatic precession						1.5875	2.5496	2.5497
						(0.2379)	(0.5381)	(0.5381)
$\cos(0.0016\,t)$				-0.0555				
				(0.0046)				
$\sin(0.0016\,t)$				0.0321				
				(0.0068)				
$\cos(0.0028\,t)$	-0.1098							
	(0.0046)							
$\sin(0.0028\,t)$	-0.4044							
	(0.0075)							
$\cos(0.0035\,t)$		0.2174						
		(0.0056)						
$\sin(0.0035\,t)$		0.0418						
		(0.0089)						
$\cos(0.0037\,t)$				-0.0241	-0.0325	0.5070		
				(0.0046)	(0.0075)	(0.0871)		
$\sin(0.0037\,t)$				-0.0821		-0.1365		
				(0.0046)		(0.0271)		
$\cos(0.0091\,t)$					-0.0954			
					(0.0056)			
$\sin(0.0091\,t)$					0.0167			
					(0.0061)			
$\cos(0.0097\,t)$			-0.0821					
			(0.0047)					
$\sin(0.0097\,t)$			-0.0986					
			(0.0048)					
$\sin(0.0777\,t)$		0.0465						
		(0.0060)						
$\sin(0.3159\,t)$		0.0248						
		(0.0059)						
$\cos(0.2451\,t)$							-0.0473	-0.0473
							(0.0167)	(0.0167)
$\cos(0.7625\,t)$							0.1123	0.1123
							(0.0172)	(0.0172)
$\cos(0.77\,t)$							-0.0606	-0.0606
							(0.0183)	(0.0183)
$\cos(1.3275\,t)$					0.0208			
					(0.0055)			
R^2	0.624	0.501	0.785	0.273	0.602	0.253	0.609	0.609
BIC	-1987.40	-1241.70	-1782.02	-1476.71	-1356.64	-771.21	351.79	351.80

Note: Standard errors are shown in parentheses.

Table 4: Segment-wise deterministic long-run models for δ^{13}C. Deterministic segmented trend models with contemporaneous cyclical trends (deterministic and from orbital variables).

Regressor	Segment 1	Segment 2	Segment 3	Segment 4	Segment 5	Segment 6	Segment 7	Segment 7 (La2004)
Constant	-118.4375	59.9326	-36.4958	0.6050	-61.0119	4.4114	-4.2941	-4.2941
	(12.8175)	(12.8548)	(8.3238)	(0.0125)	(12.2506)	(0.9726)	(0.6434)	(0.6434)
Linear trend	-0.0001	-0.0005	0.0002	0.0001	-0.0037	-0.0180	-0.0004	-0.0004
	(0)	(0)	(0)	(0)	(0.0003)	(0.0025)	(0.0001)	(0.0001)
Eccentricity	-5.1259			-5.0255				
	(0.3717)			(0.3250)				
Eccentricity × obliquity		-0.1699	-0.1725		-0.1201	-0.2034		
		(0.0245)	(0.0125)		(0.0183)	(0.0224)		
Obliquity	10.3759	-5.1127	3.1829		5.5191	0.0879	0.1685	0.1685
	(1.1081)	(1.1100)	(0.7180)		(1.0519)	(0.0138)	(0.0276)	(0.0276)
Obliquity^2	-0.2241	0.1106	-0.0684		-0.1185			
	(0.0239)	(0.0240)	(0.0155)		(0.0226)			
Climatic precession								
$\cos(0.0028\,t)$	0.2083							
	(0.0068)							
$\sin(0.0028\,t)$	-0.4991							
	(0.0111)							
$\cos(0.0031\,t)$				0.0590				
				(0.0103)				
$\sin(0.0031\,t)$				0.1012				
				(0.0092)				
$\cos(0.0035\,t)$		0.2687						
		(0.0074)						
$\sin(0.0035\,t)$		-0.5647						
		(0.0118)						
$\cos(0.0037\,t)$				0.1139	-1.7053	-6.4163		
				(0.0090)	(0.1828)	(0.8951)		
$\sin(0.0037\,t)$				0.2360	-2.7481	1.5297		
				(0.0100)	(0.2600)	(0.1860)		
$\sin(0.0046\,t)$					1.8266			
					(0.2036)			
$\cos(0.0072\,t)$			-0.1272					
			(0.0054)					
$\sin(0.0072\,t)$			0.0198					
			(0.0056)					
$\sin(0.0085\,t)$						0.8870		
						(0.1201)		
$\sin(0.0768\,t)$				-0.0390				
				(0.0060)				
$\cos(0.0777\,t)$		-0.0369						
		(0.0089)						
$\sin(0.0777\,t)$		0.0522						
		(0.0081)						
$\cos(0.0193\,t)$							0.1022	0.1022
							(0.0190)	(0.0190)
$\cos(0.3186\,t)$							-0.0935	-0.0935
							(0.0191)	(0.0191)
$\cos(0.77\,t)$							0.0689	0.0689
							(0.0209)	(0.0209)
$\cos(0.7843\,t)$					-0.0248			
					(0.0080)			
R^2	0.729	0.700	0.446	0.526	0.545	0.240	0.148	0.148
BIC	-248.17	-227.52	-1081.88	380.63	-352.91	-379.57	515.93	515.93

Note: Standard errors are shown in parentheses.

Segment-wise forecasting models

Table 5: Dynamic models for the detrended and cyclically adjusted variables: equation for δ^{18}O residuals.

Regressor	Segment 1	Segment 2	Segment 3	Segment 4	Segment 5	Segment 6	Segment 7	Out-of-sample
Constant	15.2460	-0	-0.0003	-13.2391	-0.0162	0.3248	0.0022	-0.0009
	(8.6707)	(0.0020)	(0.0016)	(4.5402)	(0.0085)	(0.1228)	(0.0094)	(0.0089)
Lagged residual $\delta^{18}O$, $t-1$	0.5189	0.5411	0.7564	0.6009	0.5380	0.2239	0.5079	0.5379
	(0.0208)	(0.0238)	(0.0199)	(0.0158)	(0.0281)	(0.0394)	(0.0433)	(0.0409)
Lagged residual $\delta^{18}O$, $t-2$	0.2847	0.2029	0.1154	0.1452	0.0435	0.1229	0.0415	0.0091
	(0.0208)	(0.0236)	(0.0199)	(0.0158)	(0.0277)	(0.0394)	(0.0433)	(0.0410)
Current residual $\delta^{13}C$, t	0.4383	0.6334	0.5745	0.3326	0.2166	0.0405	-0.1938	-0.2243
	(0.0239)	(0.0159)	(0.0190)	(0.0173)	(0.0248)	(0.0352)	(0.0339)	(0.0310)
Lagged residual $\delta^{13}C$, $t-1$	-0.1822	-0.3753	-0.4628	-0.1811	-0.1175	-0.0639	0.0397	0.0842
	(0.0292)	(0.0243)	(0.0271)	(0.0211)	(0.0301)	(0.0367)	(0.0377)	(0.0345)
Lagged residual $\delta^{13}C$, $t-2$	-0.2374	-0.1474	-0.0941	-0.0841	-0.0315	0.0315	0.0171	-0.0037
	(0.0254)	(0.0215)	(0.0222)	(0.0181)	(0.0255)	(0.0347)	(0.0343)	(0.0315)
Eccentricity, $t-2$					10.9628			
					(2.5103)			
Eccentricity × obliquity interaction, t					0.4058			
					(0.1087)			
Eccentricity × obliquity interaction, $t-1$					-0.8495			
					(0.2060)			
Obliquity, t	6.9603							
	(0.5976)							
Obliquity, $t-1$	-4.3031							
	(0.6373)							
Obliquity, $t-2$	-4.0196			1.1489				
	(0.5995)			(0.3912)				
Obliquity^2, t	-0.1489							
	(0.0129)							
Obliquity^2, $t-1$	0.0909							
	(0.0139)							
Obliquity^2, $t-2$	0.0884			-0.0249		-0.0006		
	(0.0130)			(0.0084)		(0.0002)		
Climatic precession, t				-0.3725				
				(0.0995)				
R^2	0.607	0.756	0.766	0.547	0.370	0.096	0.397	0.414
BIC	-3909.85	-3554.29	-5351.19	-4609.85	-1841.74	-789.31	-55.18	-33.32

Note: Standard errors are shown in parentheses.
Out-of-sample values refer to the specification for the next 100 kyr using La2004.

Table 6: Dynamic models for the detrended and cyclically adjusted variables: equation for δ^{13}C residuals.

Regressor	Segment 1	Segment 2	Segment 3	Segment 4	Segment 5	Segment 6	Segment 7	Out-of-sample
Constant	-6.6015	28.2312	8.8940	0.0062	-23.9045	-1.457	-1.5255	0.0023
	(7.3478)	(5.4486)	(3.8847)	(0.0044)	(12.9819)	(0.2727)	(0.5207)	(0.0107)
Current residual $\delta^{18}O$, t	0.3144	0.7566	0.4492	0.2575	0.2342	0.0517	-0.2733	-0.3213
	(0.0171)	(0.0191)	(0.0153)	(0.0134)	(0.0291)	(0.0450)	(0.0496)	(0.0454)
Lagged residual $\delta^{18}O$, $t-1$	-0.2032	-0.3662	-0.3371	-0.2255	-0.2055	-0.0450	-0.1094	-0.1080
	(0.0195)	(0.0284)	(0.0210)	(0.0159)	(0.0336)	(0.0456)	(0.0580)	(0.0553)
Lagged residual $\delta^{18}O$, $t-2$	-0.0935	-0.1936	-0.0874	-0.0146	0.0003	-0.0510	0.0454	0.0537
	(0.0183)	(0.0259)	(0.0176)	(0.0141)	(0.0297)	(0.0448)	(0.0521)	(0.0493)
Lagged residual $\delta^{13}C$, $t-1$	0.6321	0.6390	0.8136	0.6583	0.6463	0.3328	0.4101	0.4048
	(0.0208)	(0.0238)	(0.0198)	(0.0155)	(0.0276)	(0.0394)	(0.0418)	(0.0386)
Lagged residual $\delta^{13}C$, $t-2$	0.3058	0.1841	0.1130	0.2404	0.1835	0.1233	0.0334	0.0155
	(0.0209)	(0.0235)	(0.0199)	(0.0155)	(0.0268)	(0.0390)	(0.0416)	(0.0381)
Eccentricity, $t-1$			-14.7022					
			(5.1619)					
Eccentricity × obliquity interaction, $t-1$			0.7094	0.0845				
			(0.2233)	(0.0251)				
Eccentricity × obliquity interaction, $t-2$			-0.0805	-0.0947				
			(0.0193)	(0.0251)				
Obliquity, t	-10.5693		-2.4678		-3.5942			
	(0.4687)		(0.289)		(0.8179)			
Obliquity, $t-1$	7.6391		1.7218		2.5946		0.0657	
	(0.5196)		(0.2895)		(0.8467)		(0.0223)	
Obliquity, $t-2$	3.5179	-2.4807			3.0193	0.0627		
	(0.5074)	(0.4780)			(0.8236)	(0.0117)		
Obliquity^2, t	0.2278		0.0531		0.0776			
	(0.0101)		(0.0062)		(0.0176)			
Obliquity^2, $t-1$	-0.1644		-0.0375		-0.0557			
	(0.0113)		(0.0062)		(0.0184)			
Obliquity^2, $t-2$	-0.0765	0.0535			-0.0645			
	(0.011)	(0.0103)			(0.0177)			
Climatic precession, t							-2.0814	-1.9512
							(0.5148)	(0.4930)
R^2	0.859	0.830	0.853	0.785	0.670	0.221	0.371	0.364
BIC	-4613.10	-3242.39	-5923.12	-5608.89	-1654.48	-633.58	155.82	214.08

Notes: Standard errors are shown in parentheses.
Out-of-sample values refer to the specification for the next 100 kyr using La2004.

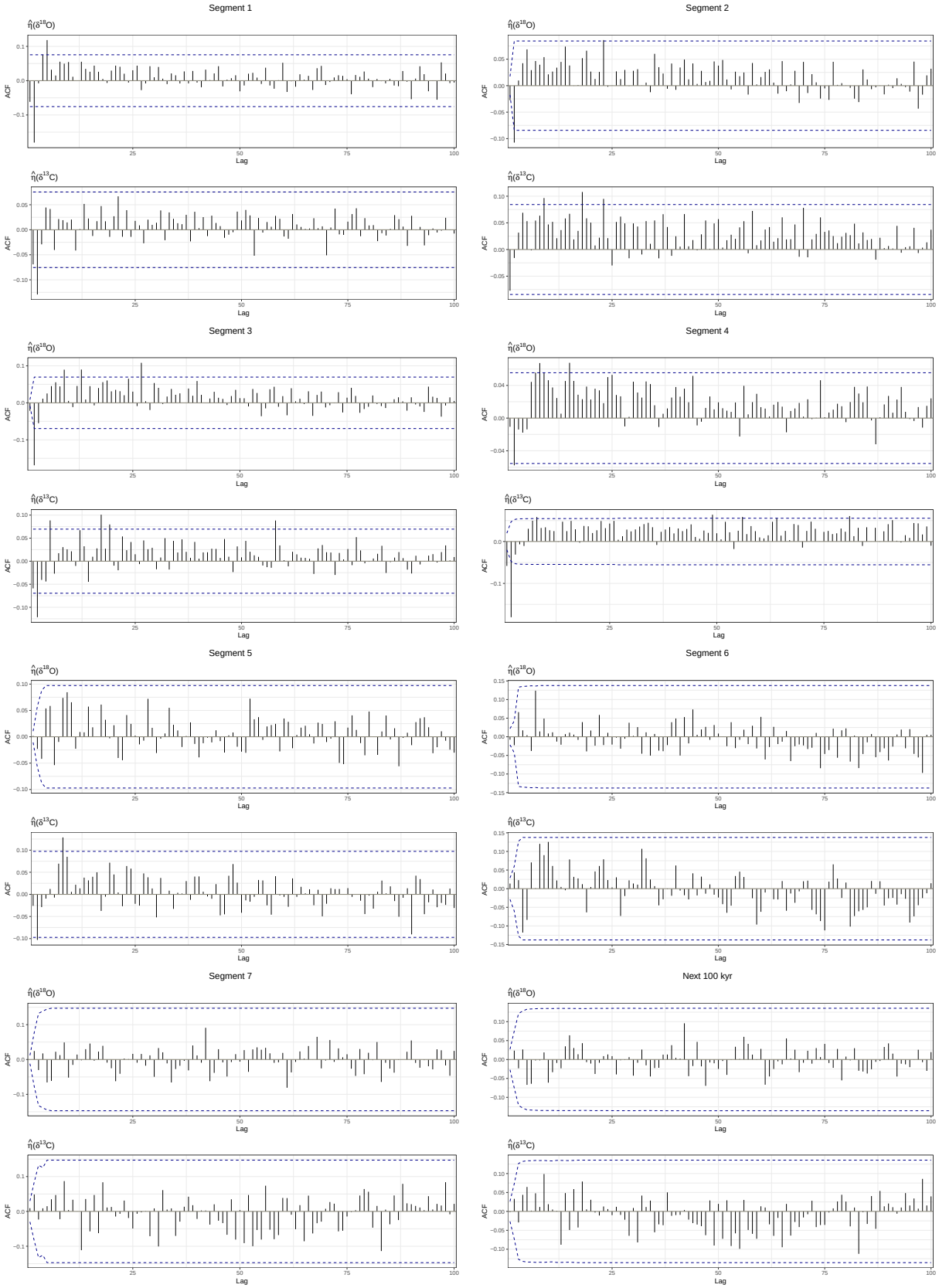

Figure 7: ACF plots for $\hat{\eta}(\delta^{18}\mathrm{O})$ and $\hat{\eta}(\delta^{13}\mathrm{C})$, Segments 1–7 and Out-of-Sample (next 100 kyr) using method by Hassler et al. (2025).

References

Bauwens, Luc, Guillaume Chevillon, and Sébastien Laurent (2023). "We modeled long memory with just one lag!" In: *Journal of Econometrics* 236(1), p. 105467.

Braconnot, Pascale, Sandy P. Harrison, Masa Kageyama, Patrick J. Bartlein, Valérie Masson-Delmotte, Ayako Abe-Ouchi, Bette Otto-Bliesner, and Yan Zhao (2021). "Paleoclimate". In: *Climate Change 2021: The Physical Science Basis. Contribution of Working Group I to the Sixth Assessment Report of the Intergovernmental Panel on Climate Change*. Ed. by Valérie Masson-Delmotte, Panmao Zhai, Anna Pirani, et al. Cambridge University Press. Chap. 2, pp. 295–408. DOI: 10.1017/9781009157896.004.

Castle, Jennifer L. and David F. Hendry (2020). "Climate Econometrics: An Overview". In: *Foundations and Trends in Econometrics* 10(3-4), pp. 145–322. ISSN: 1551-3076. DOI: 10.1561/0800000037.

Chevillon, Guillaume, Alain Hecq, and Sébastien Laurent (2018). "Generating univariate fractional integration within a large VAR (1)". In: *Journal of Econometrics* 204(1), pp. 54–65.

del Barrio Castro, Tomás, Álvaro Escribano, Yeliz Özer, and Philipp Sibbertsen (2026). *Frequency-Specific Coupling in Cenozoic Climate Variability*. Tech. rep. 749.

del Barrio Castro, Tomás, Álvaro Escribano, and Philipp Sibbertsen (2025). "Modeling and forecasting the long memory of Cyclical Trends in paleoclimate data". In: *Energy Economics*, p. 108520.

Hassler, Uwe, Marc-Oliver Pohle, and Tanja Zahn (2025). "Simultaneous Inference Bands for Autocorrelations". In: *arXiv preprint arXiv:2503.18560*.

Laskar, Jacques, Philippe Robutel, Frédéric Joutel, Mickael Gastineau, Alexandre CM Correia, and Benjamin Levrard (2004). "A long-term numerical solution for the insolation quantities of the Earth". In: *Astronomy & Astrophysics* 428(1), pp. 261–285.

Lunt, Daniel J, Bette L Otto-Bliesner, Chris Brierley, Alan Haywood, Gordon N Inglis, Kenji Izumi, Masa Kageyama, Darrell Kaufman, Thorsten Mauritsen, Erin L McClymont, et al. (2024). "Paleoclimate data provide constraints on climate models' large-scale response to past CO2 changes". In: *Communications Earth & Environment* 5(1), p. 419.

Tierney, Jessica E, Christopher J Poulsen, Isabel P Montañez, Tripti Bhattacharya, Ran Feng, Heather L Ford, Bärbel Hönisch, Gordon N Inglis, Sierra V Petersen, Navjit Sagoo, et al. (2020). "Past climates inform our future". In: *Science* 370(6517), eaay3701.

Westerhold, Thomas, Norbert Marwan, Anna Joy Drury, Diederik Liebrand, Claudia Agnini, Eleni Anagnostou, James SK Barnet, Steven M Bohaty, David De Vleeschouwer, Fabio Florindo, et al. (2020). "An astronomically dated record of Earth's climate and its predictability over the last 66 million years". In: *Science* 369(6509), pp. 1383–1387.